Physica B 628 (2022) 413624

Contents lists available at ScienceDirect

Physica B: Physics of Condensed Matter

journal homepage: www.elsevier.com/locate/physb

Studies on synthesis, structure and physical properties of $NbMoO_4$

Yu Ji [a,b], Weipeng Wang [a], Yifan Ding [a,b], Huaixiang Wang [a,b], Junkai Yang [a,b], Qinwen Guo [a,b], Xubin Ye [a,b], Xi Shen [a,**], Yuan Yao [a], Jianfa Zhao [a], Changqing Jin [a,b], Ting-Shan Chan [c], Zhiwei Hu [d], Youwen Long [a,b], Richeng Yu [a,b,e,*]

[a] Beijing National Laboratory of Condensed Matter Physics, Institute of Physics, Chinese Academy of Sciences, Beijing, 100190, PR China
[b] School of Physical Sciences, University of Chinese Academy of Sciences, Beijing, 100049, PR China
[c] National Synchrotron Radiation Research Center, 101 Hsin-Ann Road, Hsinchu, 30076, Taiwan
[d] Max Planck Institute for Chemical Physics of Solids, Dresden, 01187, Germany
[e] Songshan Lake Materials Laboratory, Dongguan, Guangdong, 523808, PR China

ARTICLE INFO

Keywords:
$NbMoO_4$
Density functional theory
Transport property
Magnetic property

ABSTRACT

A transition metal oxide, $NbMoO_4$, is synthesized by using a solid-state reaction method, then the morphology of the sample is characterized by the scanning electron microscopy. The X-ray diffraction refinement and transmission electron microscopy results show that the sample has a TiO_2 rutile-type structure with space group $P4_2/mnm$, which is the high-temperature phase of NbO_2 and MoO_2. Our transport result indicates that the resistivity is as low as 0.02 Ω·cm in the temperature range from 2 to 300 K, indicating the metallicity of $NbMoO_4$. Furthermore, the calculated density of states and experimental specific heat data from 2 to 20 K also confirm the metallic behavior. Our magnetization experiments indicate that the $NbMoO_4$ exhibits paramagnetism. The valence states of Nb^{4+} and Mo^{4+} in $NbMoO_4$ are revealed by the X-ray absorption spectroscopy.

1. Introduction

Transition metal oxides (TMOs) have attracted many scientists' attention due to their unique interactions among lattice, charges, spins, and orbitals [1], which have wide and successful applications [2] in recent decades, such as in high-T_c superconductors [3], spintronic devices, magnetoelectric and multiferroic materials [4,5]. The crystal field causes the *d*-orbitals of transition metal ions to split into t_{2g} and e_g orbitals and the Jahn-Teller distortion [6–8] further induces the removal of the degeneracy of t_{2g} and e_g orbitals. Therefore, the occupation of *d*-orbital electrons causes a metallic or insulated phase [9].

Among TMOs, the mixed transition metal dioxides, including TiO_2–NbO_2, VO_2–MoO_2, MoO_2–CrO_2, $Ti_{1-x}V_xO_2$, $V_{1-x}Nb_xO_2$ [10,11], $VMoO_4$, $TaWO_4$, $VCrO_4$, VWO_4 [12], possess structural transitions, diverse magnetic structures, metal-insulator transition, charge ordering, etc. [13–15]. Moreover, since the formation of ionic or covalent bonds occurs in the outermost *s*-orbital and *d*-orbital, there are multiple ionic valence states in the TMOs, for example, $Fe_xMo_6S_8$ [16], $Mo_{1-x}W_xS_2$ [17], Zn_3MoN_4 [18], $FeMoO_4$ [19]. The Nb and Mo ions in the TMOs have multiple valence states, indicating their diverse electronic structures.

NbO_2 has a structural transition induced by temperature from a body-centered tetragonal structure ($I4_1/a$) to a rutile structure ($P4_2/mnm$) at 1080 K [20]. MoO_2 possesses a monoclinic structure (a distorted rutile structure, space group $P2_1/c$) at room temperature and transforms into a rutile structure ($P4_2/mnm$) at 1533 K [21]. Hence, the rutile structure usually exists at high temperatures for both NbO_2 and MoO_2.

Generally, a structural transition is accompanied by a change of electrical transport properties. At room temperature, NbO_2 with a body-centered tetragonal structure maintains Nb–Nb dimer along the *c*-axis and exhibits insulator conductivity. At the structural transition temperature (1080 K), the Nb–Nb dimer breaks down and NbO_2 shows a metallic state, i.e., NbO_2 undergoes an insulator-to-metal Peierls transition. In contrast, MoO_2 keeps a metallic state with Mo–Mo dimer at room temperature. The origin of forming transition metal cation dimers is investigated in Ref. [22].

Recently, Qin et al. revealed the photoinduced insulator-to-metal transition in NbO_2 and studied the pressure effect on the electrical transport property of MoO_2 [21]. In addition, when doping with potassium (K) into MoO_2, abnormal magnetic properties compared to pure

* Corresponding author. Beijing National Laboratory of Condensed Matter Physics, Institute of Physics, Chinese Academy of Sciences, Beijing, 100190, PR China
** Corresponding author.
E-mail addresses: xshen@iphy.ac.cn (X. Shen), rcyu@iphy.ac.cn (R. Yu).

https://doi.org/10.1016/j.physb.2021.413624
Received 11 October 2021; Received in revised form 13 December 2021; Accepted 17 December 2021
Available online 20 December 2021

MoO_2 were found [23].

$NbMoO_4$ with a rutile-type structure was first synthesized in the 1950s [10,11,24]. Compared with other mixed TMOs, such as TiO_2–NbO_2, TiO_2–MoO_2, NbO_2–CrO_2 and VO_2–CrO_2, the $NbMoO_4$ was synthesized at the temperature about 1273 K, which is the synthesis condition for most of other TMOs except for TiO_2–MoO_2 (at 1573 K) [10]. Whether the synthesized TiO_2–NbO_2 by using rutile structure TiO_2 or NbO_2–MoO_2 formed by the superstructure of disordered rutile NbO_2 show a wide range of intermediary regions of ideal rutile structure [11]. Among these compounds, $NbMoO_4$ has the largest a and smaller c [10]. However, the details and physical properties of $NbMoO_4$ have been seldom studied. In this work, we synthesized $NbMoO_4$ with 4d electrons by using an improved method than before [10,11], studied the structure and physical properties in detail, and analyzed the valence states of Nb and Mo.

2. Experimental section

2.1. Sample synthesis

Polycrystalline $NbMoO_4$ samples were synthesized by using a traditional solid-state reaction method. According to the chemical equation $Nb_2O_5 + Mo + MoO_3 = 2NbMoO_4$, the raw materials Nb_2O_5, Mo and MoO_3 powders were mixed at a molar ratio of 1: 1: 1, and then pressed into a pellet and sealed in an evacuated quartz tube. Finally, the pellet was sintered for 48 h step by step at 1223 K, 1423 K, and 1273 K, respectively, with intermediate grinding.

2.2. Sample characterization

The morphology of $NbMoO_4$ was characterized by a scanning electron microscope (SEM, XL30 S-FEG). The X-ray powder diffraction (XRD) measurement was performed on a Huber diffractometer (Cu Kα1 radiation) based on the focusing principle of Seemann-Bohlin. The XRD Rietveld refinement was carried out by using the FullProf.2k program [25]. The selected area electron diffraction (SAED) patterns were acquired on transmission electron microscopes (TEMs) (CM200 with a field-emission gun (FEG), and JEM-2100 Plus) operating at 200 kV. Scanning transmission electron microscopy (STEM) studies were carried out on a JEOL ARM200F TEM equipped with double Cs correctors (CEOS) for the condenser lens and objective lens. The high-angle annular dark-field (HAADF) images and annular bright-field (ABF) images were acquired simultaneously at acceptance angles of 90–370 and 11.5–23.0 mrad, respectively. The available spatial resolution for each of the STEM images is better than 78 picometers at 200 kV. The magnetic properties were measured by using a vibrating sample magnetometer with a superconducting quantum interference device (SQUID VSM). A physical property measurement system (PPMS) was used to gain the specific heat and electrical transport data. Theoretical calculations for the density of states (DOS) were carried out using the WIEN2k package. The calculated method is a full-potential linearized augmented plane-wave (FLAPW). The used exchange-correlation functional is generalized gradient approximation (GGA) [26]. The muffin-tin radius for Mo, Nb, and O is 1.89, 1.89, and 1.71 bohr, respectively. The X-ray absorption spectroscopy (XAS) was adopted for determining the valence states of Nb and Mo at beamline BL16A of the National Synchrotron Radiation Research Center (NSRRC) in Taiwan, using a total electron yield (TEY) mode.

3. Result and discussion

Fig. 1 (a) is an SEM image of $NbMoO_4$ and shows the polycrystalline sample with an irregular quadrilateral shape, clean surface, and grain size of about 5 μm. The XRD pattern of $NbMoO_4$ at room temperature with the Rietveld refinement profile is presented in Fig. 1 (c) and all the diffraction peaks can be indexed to a TiO_2 rutile-type structure with a space group of $P4_2/mnm$ (No. 136). Specifically, this structure is the high-temperature structure of NbO_2 and MoO_2, which is transformed from the distorted rutile-type structure with a pairing of metal atoms parallel to the rutile c-axis [27]. Fig. 1 (b) shows the corresponding structure model. The mixed Nb and Mo ions occupy the Ti^{4+} position, consistent with the report in Ref. [10]. Nb and Mo ions are positioned at the 2a (0,0,0) site, and O ion is at the 4f (0.2879(4), 0.2879(4), 0) site. The refinement residuals R_p and R_{wp} are 4.52% and 6.80%, respectively, indicating a reasonable fitting result. The refined results, such as the key bond lengths and angles, are listed in Table 1.

Fig. 2 (a) and 2 (b) are the typical SAED patterns of $NbMoO_4$ along the [001] and [111] zone axes, respectively. And the corresponding

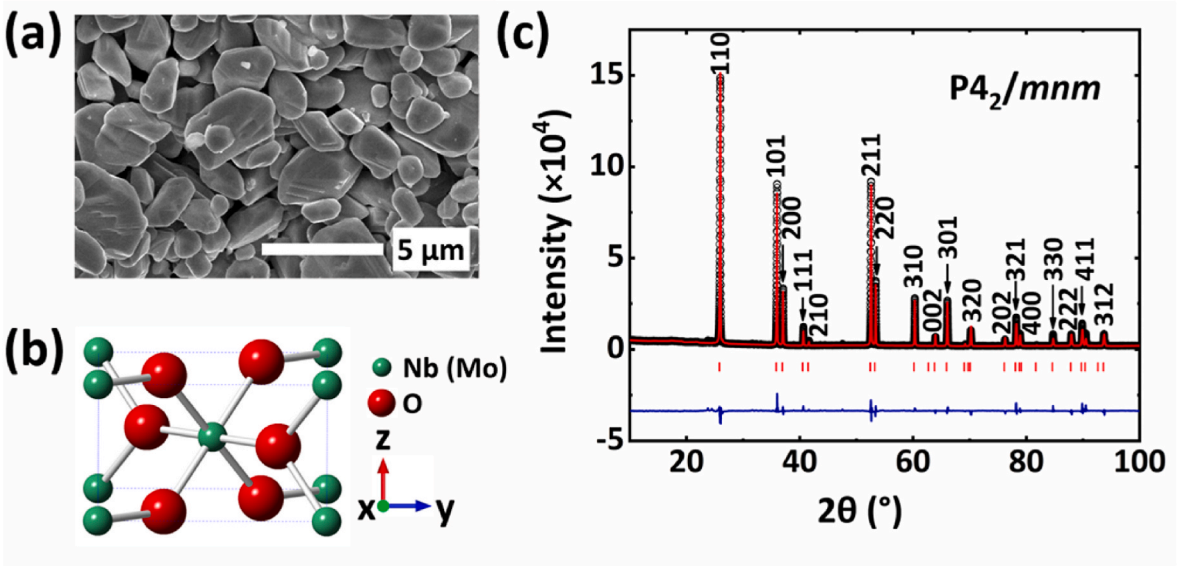

Fig. 1. (a) The SEM image of polycrystalline $NbMoO_4$. (b) The crystal structure schematic diagram of $NbMoO_4$. (c) The XRD pattern and the Rietveld refinement profile of $NbMoO_4$ at room temperature. The experimental curve (black circles), the calculated results (red line), and the differences (blue line) are displayed. The positions of the Bragg reflection peaks are marked by red ticks. The refined space group is $P4_2/mnm$. (For interpretation of the references to colour in this figure legend, the reader is referred to the Web version of this article.)

Table 1
Refinement structural parameters of $NbMoO_4$.

Parameters	$NbMoO_4$
lattice system	tetragonal
space group	$P4_2/mnm$
a (Å)	4.8499(6)
c (Å)	2.9097(5)
V (Å^3)	68.439(1)
Nb (Mo)	2a (0,0,0)
O	4f (x, x,0)
	x = 0.2879(4)
U_{iso} (Nb) (100 × Å^2)	0.483(16)
U_{iso} (Mo) (100 × Å^2)	0.483(16)
U_{iso} (O) (100 × Å^2)	0.220(58)
Nb (Mo)–O (Å)	1.9739(19)
	2.0579(14)
O–Nb (Mo)–O (°)	90.00(12)
	180.00(18)
	89.98(5)
R_{wp} (%)	6.80
R_p (%)	4.52

HAADF images at the atomic scale are shown in Fig. 2 (c) and 2 (d). The bright spots in the images indicate the positions of Nb (Mo) atomic columns. Since the contrast intensity of HAADF images is approximately proportional to $Z^{1.5}$ (Z is an atomic number) [28–30], the contrast of Nb (Z = 41) and Mo (Z = 42) atoms is indistinguishable in Fig. 2 (c) and 2 (d). Nevertheless, the HAADF images still provide direct evidence of the rutile structure of $NbMoO_4$. Fig. 2 (e) and 2 (f) present the corresponding ABF images along the [001] and [111] zone axes, respectively. The enlarged details of ABF images superimposed with the refined structure along the corresponding zone axes are displayed in Fig. 2 (g) and 2 (h). The above results indicate that $NbMoO_4$ at room temperature has the high-temperature phase of NbO_2 and MoO_2.

The resistivity curve versus temperature is displayed in Fig. 3. The magnitude of resistivity lies in the level of 10^{-2} Ω·cm, to more precise, the resistivity has a little change from 24.2 mΩ·cm to 18.7 mΩ·cm with increasing temperature from 2 to 300 K. The tendency of resistivity reducing with increasing temperature may be caused by the grain boundary effect in the polycrystalline sample. The transport properties indicate that the rutile-type structural $NbMoO_4$ is metallic, similar to the high-temperature phase of NbO_2 [31]. It should be noted that both of the phases have no cation dimers. We further calculated the density of states (DOS) to study the electronic property of $NbMoO_4$ and present the related results in Fig. 4 (b).

We calculated the DOS of $NbMoO_4$ as well as MoO_2 for comparison. The calculated DOS of MoO_2 with Coulomb interactions U=4 eV to the Mo atom is shown in Fig. 4 (a). The DOS at the Fermi surface is nonzero as shown in Fig. 4 (a), which means the metallic conductivity. Our result coincides with the previous report in Ref. [27]. We use the virtual crystal approximation method to calculate the DOS of $NbMoO_4$. All the results show the metallicity of $NbMoO_4$ as U values applied to the Nb and Mo atoms changes from 0 eV to 6 eV at the interval of 2 eV. As an example, Fig. 4 (b) presents the calculation result of U=4 eV. Even if the Coulomb interactions energy up to 6 eV, the calculated result still manifests as a metallic state, which means that $NbMoO_4$ is intrinsically metallic. In addition, we also performed calculations for four types of large supercells consist of 72 atoms, with the random distribution of Nb and Mo atoms. In the calculations, we applied the total 60 k-points in the Brillouin zone. The calculated results show that the refined structures (shown in Fig. S1) using the WIEN2k package have little changes from the constructed ones and all the DOS (shown in Fig. S2) also show metallic states. In our calculations, we applied the virtual crystal approximation as well as constructed four types of random distributions of supercells, and obtained the metallic characteristics for all the cases, consistent with our experimental results.

Furthermore, we measured specific heat c_p(T) and no obvious abnormal peak has been observed in the temperature range of 2–300 K (Fig. 5). In the range of 2–20 K, it is noticed that the data can be well fitted by the formula $c_p = \gamma T + \beta T^3$, shown in Fig. 5. The γT and βT^3 represent the electronic and the lattice heat-capacity, respectively. The value of the electronic heat capacity coefficient (γ) is estimated as 6.829 × 10^{-2} J/mol·K^2 and the lattice heat-capacity coefficient (β) is 4.687 × 10^{-4} J/mol·K^4. The fitted coefficient γ is much larger than β, which

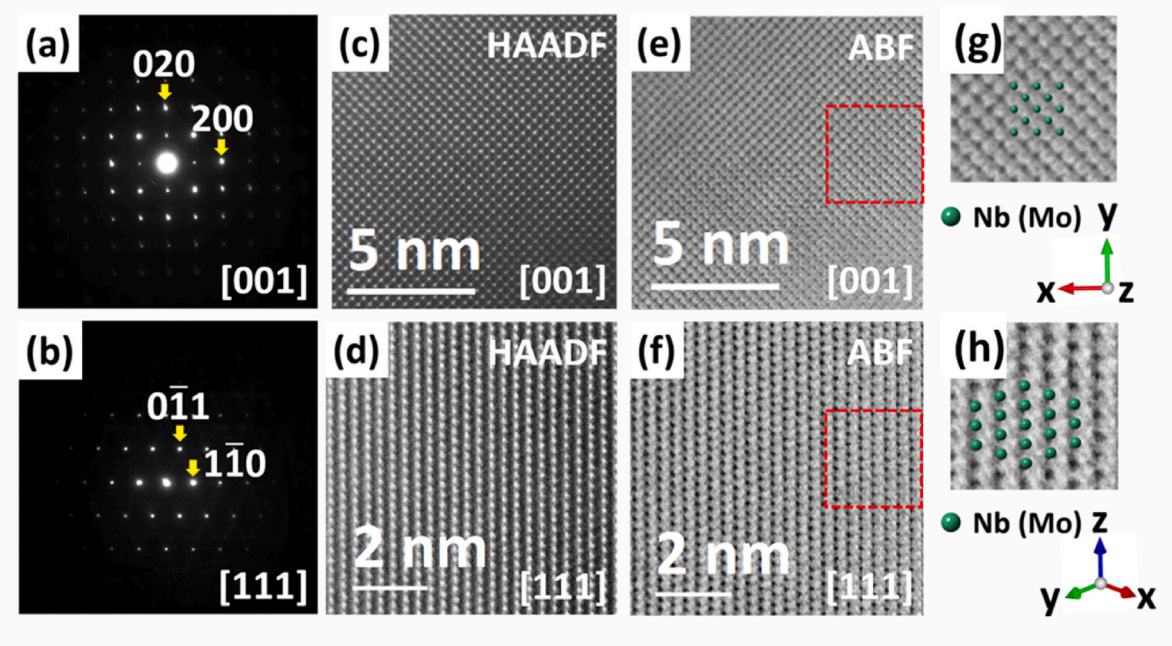

Fig. 2. (a) and (b) The SAED patterns of $NbMoO_4$ along the [001] and [111] zone axes, respectively. (c) and (d) The corresponding HAADF images along the [001] and [111] zone axes, respectively. (e) and (f) The corresponding ABF images along the [001] and [111] zone axes, respectively. (g) and (h) The enlarged details of the ABF images superimposed with the refined structure along the [001] and [111] zone axes, respectively (corresponding to the regions of red frames in (e) and (f), respectively). (For interpretation of the references to colour in this figure legend, the reader is referred to the Web version of this article.)

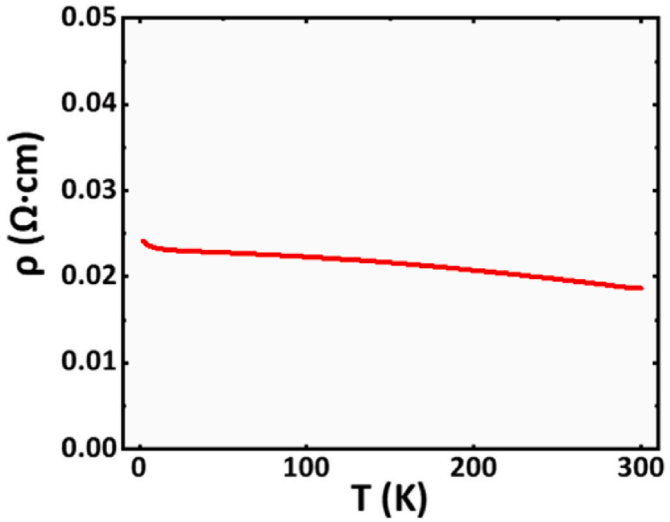

Fig. 3. The resistivity as a function of temperature for $NbMoO_4$ from 2 to 300 K.

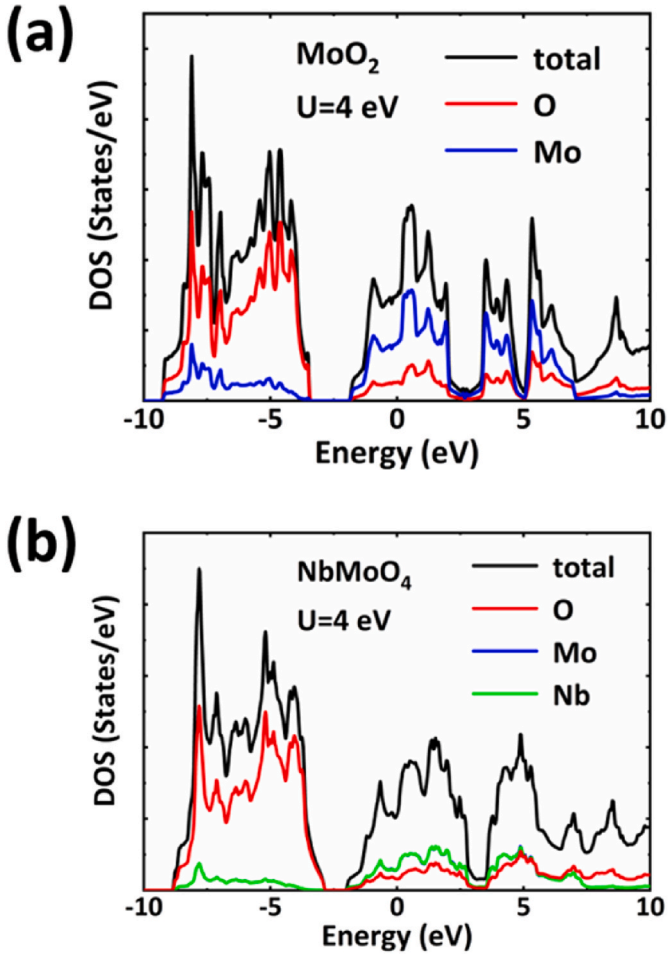

Fig. 4. (a) Calculated total and elemental DOS for Mo and O ions. (b) Calculated total and elemental DOS for Nb, Mo, and O ions.

means the electronic heat-capacity dominantly contributes to the total specific heat at low temperatures. It again confirms that $NbMoO_4$ exhibits a metallic behavior.

Magnetization as a function of temperature obtained in zero field cooled (ZFC) and field cooled (FC, H = 0.1 T) conditions for $NbMoO_4$ are

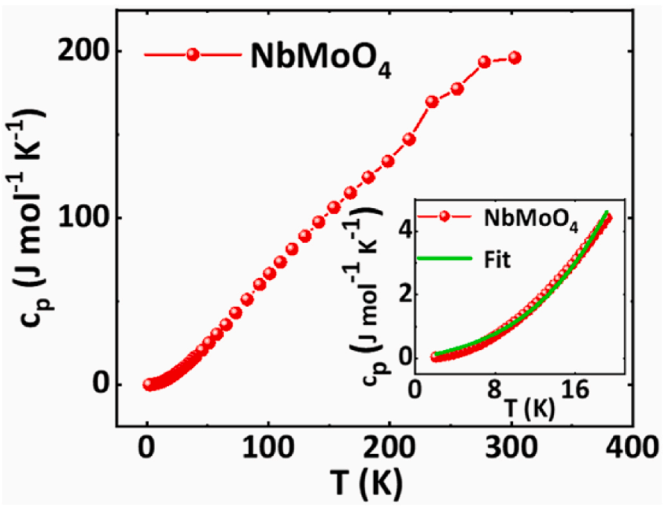

Fig. 5. The temperature dependence of specific heat $c_p(T)$ of $NbMoO_4$. The inserted image is an enlarged part of $c_p(T)$ in the temperature range of 2–20 K. The experimental data (the red curve) is fitted by the formula $c_p = \gamma T + \beta T^3$ (the green curve). (For interpretation of the references to colour in this figure legend, the reader is referred to the Web version of this article.)

displayed in Fig. 6 (a). The ZFC and FC curves were acquired at an applied magnetic field H = 0.1 T and show identical characteristics. The $1/\chi$-T curve of the ZFC is also shown in Fig. 6 (a). It is indicated that the curve does not typically obey the Curie-Weiss law that should be approximate to a straight line in a high temperature range [32]. In the case of the metallic state of $NbMoO_4$, we consider that the magnetization behavior is determined by Pauli paramagnetism and Curie-Weiss paramagnetism. As shown in Fig. 6 (a), we fit the high-temperature data from 100 to 400 K with modified Curie-Weiss law ($\chi = \frac{C}{T-\theta} + \chi_0$) and finally obtain paramagnetism result with the fitting parameters $\theta \approx 0$ K, $C = 0.0261$ emu·K·mol^{-1}·Oe^{-1} and $\chi_0 = 3.8477 \times 10^{-4}$ emu·mol^{-1}·Oe^{-1}. Fig. 6 (b) shows the hysteresis loops of $NbMoO_4$ in magnetic fields from −7 to 7 T at 2 K and 300 K, respectively. The hysteresis loop at 300 K is a straight line, indicating a typical paramagnetic behavior. The magnetization is still proportional to the applied magnetic field even up to about 1 T at 2 K, and the hysteresis loop begins to bend as H continuously increases. The shape of the hysteresis loop at 2 K conforms to the typical paramagnetic Brillouin function [33]. Based on the above results, we conclude that $NbMoO_4$ is a paramagnetic metal.

To understand the electronic structure of $NbMoO_4$, we have measured X-ray absorption spectra (XAS) at the Nb L_3 and Mo L_3 edges, which is sensitive to the valence state of 4*d* transition metal elements [34–36]. Fig. 7 (a) shows Mo L_3 XAS spectra of $NbMoO_4$ and La_2LiMoO_6 and MoO_3 as a Mo^{5+} and a Mo^{6+} reference, respectively. The lower and the higher energy peaks are related to the transition from the Mo 2*p* core level to the t_{2g} and the e_g orbitals in octahedral coordination, respectively. There is a gradual shift to the lower energy from Mo^{6+} in MoO_3 to Mo^{5+} in La_2LiMoO_6 and further to $NbMoO_4$, indicating Mo^{4+} valence state in the $NbMoO_4$. It is indicated that the Nb^{4+} valence state is confirmed due to a charge balance requirement. Fig. 7 (b) presents the Nb L_3 XAS spectra of $NbMoO_4$ together with NbO_2 and Nb_2O_5 as an Nb^{4+} and an Nb^{5+} reference, respectively. The $NbMoO_4$ and NbO_2 have nearly the same energy and are shifted to the lower energy with respect to Nb^{5+} reference Nb_2O_5, indicating Nb^{4+} valence state in $NbMoO_4$. The different spectral features between NbO_2 and $NbMoO_4$ is originated from a strong local distortion in the former [37].

4. Conclusions

We have successfully synthesized polycrystalline $NbMoO_4$ and determined its structure as a rutile type, which is the high-temperature

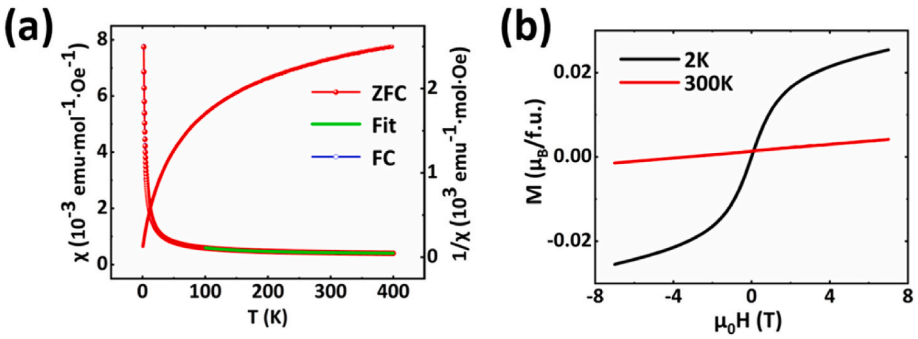

Fig. 6. (a) Temperature-dependent magnetic susceptibility and inverse magnetic susceptibility measured at H = 0.1 T from 2 to 400 K for $NbMoO_4$. The green line between 100 K and 400 K shows the modified Curie-Weiss law fitting with the function $\chi = \frac{C}{T-\theta} + \chi_0$. (b) The hysteresis loops of $NbMoO_4$ at 2 K (black curve) and 300 K (red curve), respectively. (For interpretation of the references to colour in this figure legend, the reader is referred to the Web version of this article.)

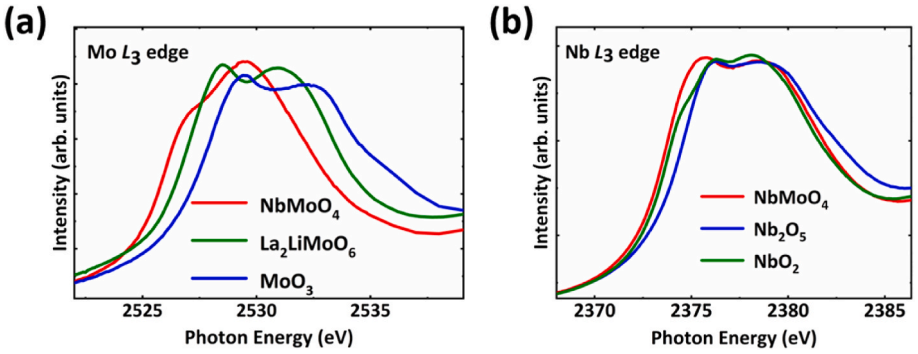

Fig. 7. XAS spectra of (a) Mo L_3 edge and (b) Nb L_3 edge. The XAS spectra of some related references are also shown for comparison.

structure of NbO_2 and MoO_2. The transport property measurement indicates that polycrystalline $NbMoO_4$ has a metallic behavior, consistent with our theoretical calculation results and the specific heat data. The metallic state with a rutile-type structure is in accordance with the high-temperature phase of NbO_2 and MoO_2. We reveal that $NbMoO_4$ is paramagnetic and both Nb and Mo ions have a +4 valence state in $NbMoO_4$.

Credit author statement

Yu Ji: Conceptualization, Investigation, Validation, Writing – original draft. Weipeng Wang: Data curation. Yifan Ding: Methodology, Software. Huaixiang Wang: Formal analysis. Junkai Yang: Writing – review & editing. Qinwen Guo: Writing – review & editing. Xubin Ye: Visualization. Xi Shen: Funding acquisition, Writing – review & editing. Yuan Yao: Investigation. Jianfa Zhao: Data curation. Changqing Jin: Resources. Ting-Shan Chan: Investigation. Zhiwei Hu: Writing – review & editing. Youwen Long: Funding acquisition, Resources. Richeng Yu: Conceptualization, Funding acquisition, Project administration, Supervision, Writing – review & editing.

Declaration of competing interest

The authors declare that they have no known competing financial interests or personal relationships that could have appeared to influence the work reported in this paper.

Acknowledgement

This work was supported by the National Key Research Program of China (Grant Nos. 2017YFA0206200, 2018YFA0208402 and 2018YFE0103200), the National Natural Science Foundation of China (Grant Nos. 11874413, 11934017 and 51972333) and the Strategic Priority Research Program of the Chinese Academy of Sciences, No. XDB33030200. X. Shen is sponsored by the Youth Innovation Promotion Association of CAS (2019009). We acknowledge support from the Max Planck-POSTECH-Hsinchu Center for Complex Phase Materials.

Appendix A. Supplementary data

Supplementary data to this article can be found online at https://doi.org/10.1016/j.physb.2021.413624.

References

[1] J.M. Rondinelli, N.A. Spaldin, Structure and properties of functional oxide thin films: insights from electronic-structure calculations, Adv. Mater. 23 (30) (2011) 3363–3381.
[2] D.I. Khomskii, Introduction, Transition Metal Compounds, Cambridge University Press, 2014, pp. Ix–Xii.
[3] G.M. Zhao, M.B. Hunt, H. Keller, K.A. Muller, Evidence for polaronic supercarriers in the copper oxide superconductors $La_{2-x}Sr_xCuO_4$, Nature 385 (6613) (1997) 236–239.
[4] V. Cuartero, J. Blasco, J. García, G. Subías, C. Ritter, J.A. Rodríguez-Velamazán, Structural effects of Sc doping on the multiferroic $TbMnO_3$, Phys. Rev. B 81 (22) (2010) 224117.
[5] K. Xu, H.J. Xiang, Unusual ferroelectricity induced by the jahn-teller effect: a case study on lacunar spinel compounds, Phys. Rev. B 92 (12) (2015) 121112.
[6] I.S. Elfimov, V.I. Anisimov, G.A. Sawatzky, Orbital ordering, Jahn-Teller distortion, and anomalous x-ray scattering in manganates, Phys. Rev. Lett. 82 (21) (1999) 4264.
[7] I.I. Mazin, D.I. Khomskii, R. Lengsdorf, J.A. Alonso, W.G. Marshall, R.M. Ibberson, A. Podlesnyak, M.J. Martinez-Lope, M.M. Abd-Elmeguid, Charge ordering as alternative to Jahn-Teller distortion, Phys. Rev. Lett. 98 (17) (2007) 176406.
[8] E. Pavarini, E. Koch, Origin of jahn-teller distortion and orbital order in $LaMnO_3$, Phys. Rev. Lett. 104 (8) (2010), 086402.
[9] I. Loa, P. Adler, A. Grzechnik, K. Syassen, U. Schwarz, M. Hanfland, G. Kh Rozenberg, P. Gorodetsky, M.P. Pasternak, Pressure-induced quenching of the Jahn-Teller distortion and insulator-to-metal transition in $LaMnO_3$, Phys. Rev. Lett. 87 (12) (2001) 125501.
[10] B.O. Marinder, E. Dorm, M. Seleborg, Studies on rutile-type phases in mixed transition metal dioxides II, Acta Chem. Scand. 16 (2) (1962) 293–296.

[11] B.O. Marinder, A. Magnéli, Rutile-type phases in some systems of mixed transition metal dioxides, Acta Chem. Scand. 12 (6) (1958) 1345–1347.
[12] A.O. Gunina, S.I. Lopatin, S.M. Shugurov, Gaseous vanadium molybdate and tungstates: thermodynamic properties and structures, Inorg. Chem. 51 (9) (2012) 4918–4924.
[13] D. Kan, R. Aso, R. Sato, M. Haruta, H. Kurata, Y. Shimakawa, Tuning magnetic anisotropy by interfacially engineering the oxygen coordination environment in a transition metal oxide, Nat. Mater. 15 (4) (2016) 432–437.
[14] M. Dekkers, G. Rijnders, D.H. Blank, $ZnIr_2O_4$, ap-type transparent oxide semiconductor in the class of spinel zinc-d 6-transition metal oxide, Appl. Phys. Lett. 90 (2) (2007), 021903.
[15] H. Guo, Z.W. Li, L. Zhao, Z. Hu, C.F. Chang, C.Y. Kuo, W. Schmidt, A. Piovano, T. W. Pi, O. Sobolev, et al., Antiferromagnetic correlations in the metallic strongly correlated transition metal oxide $LaNiO_3$, Nat. Commun. 9 (1) (2018) 1–7.
[16] A. Fujimori, M. Sekita, H. Wada, Photoemission and auger-electron spectroscopic study of the chevrel-phase compound $Fe_xMo_6S_8$, Phys. Rev. B 33 (10) (1986) 6652.
[17] H. Liu, K.K.A. Antwi, S. Chua, D. Chi, Vapor-phase growth and characterization of $Mo_{1-x}W_xS_2$ ($0 \leq x \leq 1$) atomic layers on 2-inch sapphire substrates, Nanoscale 6 (1) (2014) 624–629.
[18] E. Arca, S. Lany, J.D. Perkins, C. Bartel, J. Mangum, W. Sun, A. Holder, G. Ceder, B. Gorman, G. Teeter, et al., Redox-mediated stabilization in zinc molybdenum nitrides, J. Am. Chem. Soc. 140 (12) (2018) 4293–4301.
[19] Z. Ju, E. Zhang, Y. Zhao, Z. Xing, Q. Zhuang, Y. Qiang, Y. Qian, One-Pot hydrothermal synthesis of $FeMoO_4$ nanocubes as an anode material for lithium-ion batteries with excellent electrochemical performance, Small 11 (36) (2015) 4753–4761.
[20] M.J. Wahila, G. Paez, C.N. Singh, A. Regoutz, S. Sallis, M.J. Zuba, J. Rana, M. Brooks Tellekamp, J.E. Boschker, T. Markurt, et al., Evidence of a second-order Peierls-driven metal-insulator transition in crystalline NbO_2, Phys Rev Mater 3 (7) (2019), 074602.
[21] T.R. Qin, Q.L. Wang, D.H. Yue, H. Liu, Y.J. Zheng, Y.H. Han, C.X. Gao, The effect of pressure and temperature on the structure and electrical transport properties of MoO_2, J. Alloys Compd. 814 (2020) 152336.
[22] J.B. Goodenough, Metallic oxides, Prog. Solid State Chem. 5 (1971) 145–399.
[23] L. Alves, B.S. de Lima, C.A. dos Santos, A. Rebello, S.H. Masunaga, J.J. Neumeier, J.B. Leao, Phase transitions in K-doped MoO_2, J. Appl. Phys. 115 (20) (2014) 204912.
[24] A. Sundholm, S. Andersson, A. Magnéli, B.O. Marinder, Metal-metal bonding in a mixed chromium molybdenum oxide phase of rutile structure, Acta Chem. Scand. 12 (1958). No.6.
[25] Rodriguez-Carvajal, Satellite Meeting on Powder Diffraction of the XV Congress of the IUCr, France, Toulouse, 1990.
[26] J.P. Perdew, K. Burke, M. Ernzerhof, Generalized gradient approximation made simple, Phys. Rev. Lett. 77 (18) (1996) 3865.
[27] V. Eyert, R. Horny, K.H. Höck, S. Horn, Embedded Peierls instability and the electronic structure of MoO_2, J. Phys. Condens. Matter 12 (23) (2000) 4923.
[28] D.E. Jesson, S.J. Pennycook, Incoherent imaging of crystals using thermally scattered electrons, Proc R Soc London A: Math Phys Sci. 449 (1936) (1995) 273–293.
[29] S.J. Pennycook, D.E. Jesson, High-resolution Z-contrast imaging of crystals, Ultramicroscopy 37 (1–4) (1991) 14–38.
[30] S.J. Pennycook, Z-contrast STEM for materials science, Ultramicroscopy 30 (1–2) (1989) 58–69.
[31] G. Belanger, J. Destry, G. Perluzzo, P.M. Raccah, Electron transport in single crystals of niobium dioxide, Can. J. Phys. 52 (22) (1974) 2272–2280.
[32] Z.H. Liu, X. Wang, X.B. Ye, X.D. Shen, Y.C. Bian, W. Ding, S. Agrestini, S.C. Liao, H. J. Lin, C.T. Chen, et al., Observation of A-site antiferromagnetic and B-site ferrimagnetic orderings in the quadruple perovskite oxide $CaCu_3Co_2Re_2O_{12}$, Phys. Rev. B 103 (1) (2021), 014414.
[33] M.I. Darby, Tables of the Brillouin function and of the related function for the spontaneous magnetization, Br. J. Appl. Phys. 18 (10) (1967) 1415.
[34] T. Burnus, Z. Hu, H. Wu, J.C. Cezar, S. Niitaka, H. Takagi, C.F. Chang, N. B. Brookes, H.J. Lin, L.Y. Jang, et al., X-ray absorption and x-ray magnetic dichroism study on Ca_3CoRhO_6 and Ca_3FeRhO_6, Phys. Rev. B 77 (20) (2008) 205111.
[35] S. Nemrava, L. Link, Z. Hu, B. Blaschkowski, S.C. Liao, H.J. Lin, C.T. Chen, T. S. Chan, L.H. Tjeng, R. Niewa, Synthesis and characterization of $BaLiRu_5O_{11}$, $BaCu_{1+x}Ru_{5-x}O_{11}$, and $BaLi_{1-x}Cu_{x+\delta}Ru_{5-\delta}O_{11}$: crystal structures and valence states, J of Inorg and Gen Chem 644 (24) (2018) 1691–1696.
[36] N. Hollmann, Z. Hu, A. Maignan, A. Günther, L.Y. Jang, A. Tanaka, H.J. Lin, C. T. Chen, P. Thalmeier, L.H. Tjeng, Correlation effects in $CaCu_3Ru_4O_{12}$, Phys. Rev. B 87 (15) (2013) 155122.
[37] C. Sanloup, B. Cochain, C. Grouchy, K. Glazyrin, Z. Konôpkova, H.P. Liermann, I. Kantor, R. Torchio, O. Mathon, T. Irifune, Behaviour of niobium during early Earth's differentiation: insights from its local structure and oxidation state in silicate melts at high pressure, J. Phys. Condens. Matter 30 (8) (2018), 084004.